We are IntechOpen, the world's leading publisher of Open Access books Built by scientists, for scientists

4,800
Open access books available

122,000
International authors and editors

135M
Downloads

Our authors are among the

154
Countries delivered to

TOP 1%
most cited scientists

12.2%
Contributors from top 500 universities

WEB OF SCIENCE™

Selection of our books indexed in the Book Citation Index in Web of Science™ Core Collection (BKCI)

Interested in publishing with us?
Contact book.department@intechopen.com

Numbers displayed above are based on latest data collected.
For more information visit www.intechopen.com

Chapter 17

Feedback Regulation of Limb Position Characterized Using FMRI

Aaron J. Suminski and Robert A. Scheidt

Additional information is available at the end of the chapter

http://dx.doi.org/10.5772/30740

1. Introduction

Functional magnetic resonance imaging (FMRI) is a powerful tool for exploring the neural basis of sensory control of movement and it has profitably been used to study simple actions like finger-tapping (Rao et al., 1996), compensation for visual feedback distortions during movement (Imamizu et al., 2000) and regulation of isometric force (Peck et al., 2001; Kawato et al., 2003; Vaillancourt et al., 2003). However, use of FMRI to image neural mechanisms contributing to more complex motor tasks like stabilization of limb position in the face of environmental perturbation has been limited because such tasks require mechanically-active, MRI-compatible devices capable to perturb the limb in a controlled manner. Here, we present a case study on the development and validation of a MRI-compatible device specifically for use in studying sensorimotor control in the presence of environmental perturbations. We then demonstrate the device in a functional imaging study of limb posture regulation wherein healthy human subjects stabilized their wrists against predictable and unpredictable loads. In particular, we sought to understand how the brain uses somatosensory information to adjust behavioral strategies for load compensation.

We anticipated that multiple strategies might be used to stabilize the limb against perturbation, and that distinct neural mechanisms would implement these strategies. We therefore hypothesized that at least two distinct neural mechanisms contribute to the stabilization of wrist position in the presence of persistent environmental perturbations. A first mechanism likely mediates the online control of endpoint position (not joint torque) via feedback control. Feedback control attempts to adjust motor commands to cancel deviations of the limb from its desired state. Thus we expect regions contributing to feedback control of wrist position to show increased FMRI BOLD response in the presence of positioning errors, independent of joint torque magnitude. Moreover, temporal variations in the BOLD response in these regions

should correlate with variations in wrist position on a moment-by-moment basis. A second mechanism likely monitors performance over a longer timeframe than an online feedback controller. This mechanism would initiate discrete, conditional, corrective actions when feedback control fails to eliminate persistent errors. Regions contributing to this higher-order evaluation of performance should demonstrate BOLD responses that reflect changes in positioning errors with a longer temporal integration period than that used for moment-by-moment feedback control.

Portions of this chapter have appeared previously in separate publications (Suminski et al., 2007b; Suminski et al., 2007a).

2. Development of a MRI-compatible manipulandum

Devices intended for use in MRI environments must: 1) satisfy noise tolerance and size limitations imposed by MR scanner technologies, and 2) be constructed of MR compatible materials (Schenck, 1996; Chinzei et al.). The large static magnetic field generated by the scanner precludes use of ferromagnetic materials that would otherwise be attracted into the scanner bore, compromising safety of both the research subject and the scanner. It is also essential that all actuators and sensors in the device be impervious to rapidly switching imaging gradients and that device operation does not disturb the homogeneity of the magnetic field, which would lead to image distortion. Finally, the device must have a small form factor, capable to fit inside the scanner bore without causing subject discomfort. To date, a small number of such robotic devices have been developed for use in neuroscience research or rehabilitation applications (Suminski et al., 2002; Ganesh et al.,2004; Diedrichsen et al., 2005; Flueckiger et al., 2005; Khanicheh et al., 2005; Gassert et al., 2006; Khanicheh et al., 2008; Yu et al., 2008). In this section we describe the design, performance characteristics and validation of a novel, MR compatible, 1 degree-of-freedom (DOF), pneumatically actuated robot for motor control research (Fig. 1). Our aim was to create a device able to both monitor and perturb wrist motion during FMRI, and to demonstrate device safety and efficacy as a tool for the study of complex motor behavior in human subjects.

2.1. Device design and performance characteristics

We used a pneumatic actuator to exert computer-controlled torques about the wrist because this type of actuator can be MR compatible, small, light-weight and back-driveable. A single bellows-type actuator was enclosed within a curved volume. This actuator transmits force from compressed air to a wall rigidly attached to the device's handle. Pressurizing the actuator generates an extensor torque about the subject's right wrist whereas pulling a vacuum within the actuator imparts a flexor torque. Air pressure within the actuator is sensed by a pressure transducer (26PC Series, Honeywell International, Inc., Morristown, NJ), amplified (x25) and low-pass filtered (20Hz cutoff frequency) in hardware. Joint angle is sensed with an optical encoder (HEDM-6540, Agilent Technologies, Inc., Palo Alto, CA) located on the underside of the device. The device monitors wrist position to within 0.05° and wrist torque to within 0.001

http://dx.doi.org/10.5772/30740

Nm. Only the manipulandum, pressure transducer, optical encoder and necessary instrumentation are located within the MR environment; all other control components are located in the scanner control room. The manipulandum can accommodate both right- and left-handed individuals, providing 80° range of motion at the wrist (40° flexion to 40° extension). Pressure within the actuator is regulated by a Proportion Air QB3 electro-pneumatic pressure valve (Proportion-Air Inc., McCordsville, IN). Wrist angle and actuator pressure data are acquired at a rate of 1000 samples per second. Commands to the pressure valve are generated at the same rate.

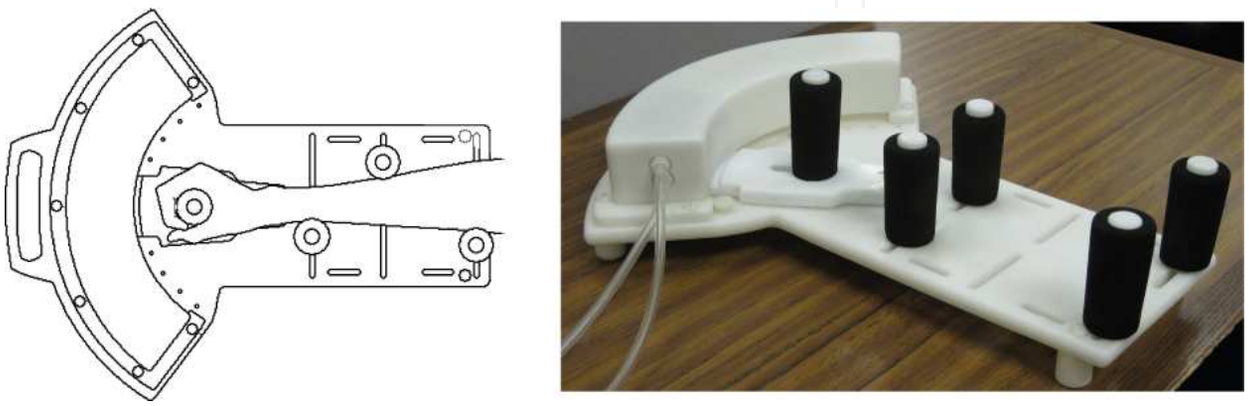

Figure 1. Schematic representation and a photograph of the 1 DOF pneumatic manipulandum.

We implemented a proportional-integral-derivative (PID) controller to improve the ability of the device to quickly and accurately regulate pressure within the pneumatic actuator.

$$P_C(t) = K_P e(t) + K_I \int e(t)dt + K_D \dot{e}(t) \quad (1)$$

where $P_C(t)$ is the commanded actuator pressure in units of psi, e(t) is the difference between the measured and desired actuator pressure in units of psi, K_P is the proportional gain, K_I is the integral gain, and K_D is the derivative gain. Ziegler-Nichols tuning rules were used to tune the controller (Ziegler and Nichols, 1942), yielding the following gain values: $K_P = 3.3$, $K_I = 14$, and $K_D = 0.055$. Under PID control, step response rise times (10% to 90% steady state) were 77ms and 90ms for 1 and 2 PSI step changes, respectively, with modest overshoot (19%; Fig. 2A). Due to time required to transmit air from the MRI control room to the actuator, we observed an average time delay (command onset to 10% steady state) of 62ms for both step responses.

We identified the bandwidth of the closed-loop system by assessing the system's ability to track changes in commanded actuator pressure having a 1 PSI peak-to-peak 'chirp' profile sweeping from 0 to 5Hz. The device is able to track commanded pressure changes within ±15% of the peak pressure up to 1.6 Hz (Fig. 2B). These frequency response characteristics allow the

robot to apply torsional spring-like loads about the wrist. By way of demonstration, we commanded the robot to apply two separate position-dependent loads (0.075 and 0.15 Nm/°) and estimated the realized spring constants obtained during 25° flexion/extension movements performed by a representative human subject. The estimated stiffness of the two spring-like loads, obtained by fitting a linear model to the joint torque vs. joint angle data, were 0.059 and 0.134 Nm/° respectively, yielding an average error of 16%. In both cases, the torque-angle relationships were linear, with regression r^2 values exceeding 96% and 99% for the 0.075 and 0.15 Nm/° loads, respectively (Fig. 2C).

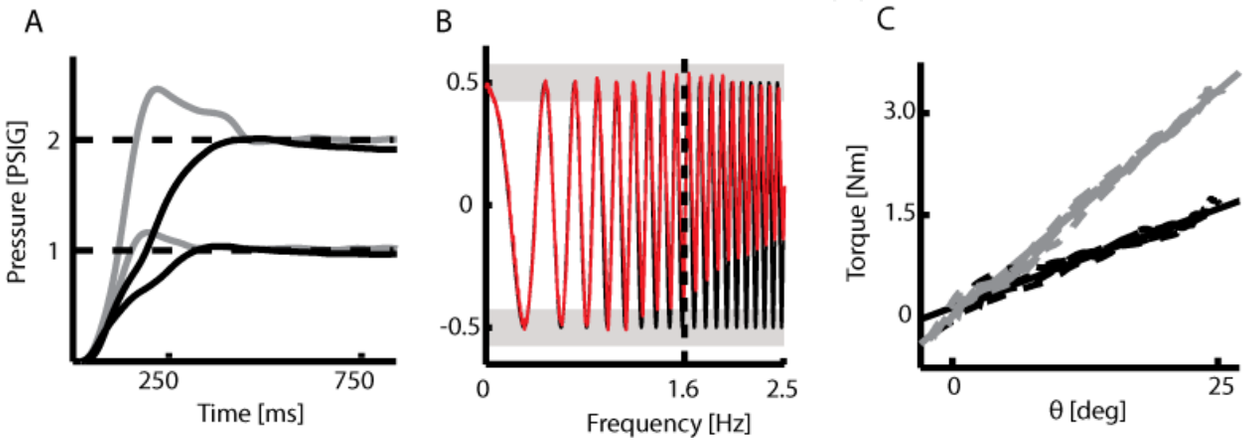

Figure 2. (A) Responses of the robot to 1 and 2 PSI step changes in pressure under open loop control (i.e. no pressure feedback to controller; black lines) and closed loop PID control (i.e. real-time feedback of actual actuator pressure to the controller; gray lines). (B) The frequency response of the system under closed loop control (red line) was identified by assessing the system's ability to track a desired actuator pressure signal sweeping from 0 to 5Hz (black line). The upper bound on the system's bandwidth was defined to be the frequency at which the controller was unable to regulate the actuator pressure within 15% of the peak commanded pressure (horizontal gray bars). (C) Spring constants for two simulated loads (0.075 and 0.15 Nm/°; dashed black and gray lines, respectively) estimated by fitting a line to the joint torque and wrist angle data (solid lines). Figure adapted from Suminski et al., 2007a.

2.2. MR-compatibility testing

We validated the simultaneous acquisition of manipulandum data and FMRI images by scanning a spherical head phantom both with and without the robotic device in a 3.0T GE Excite HD MR scanner (General Electric Healthcare, Milwaukee, WI). The phantom (Fig. 3A, P; GE Model #: 2359877) was supported within a split transmit/receive quadrature head coil (Fig. 3A, HC; GE Model #: 2376114). A gradient echo, echo planar imaging (EPI) pulse sequence (29 contiguous sagittal slices; echo time (TE) = 25ms, inter-scan period (TR) = 2s, flip angle = 77°, field of view (FOV) = 24cm, 64 x 64 matrix; 3.75x3.75x6 mm spatial resolution) was used to verify: 1) that operation of the robot during scanning does not induce significant artifacts in functional images, and 2) that the robot can measure pressure and joint angle without contamination from gradient switching noise during EPI.

http://dx.doi.org/10.5772/30740

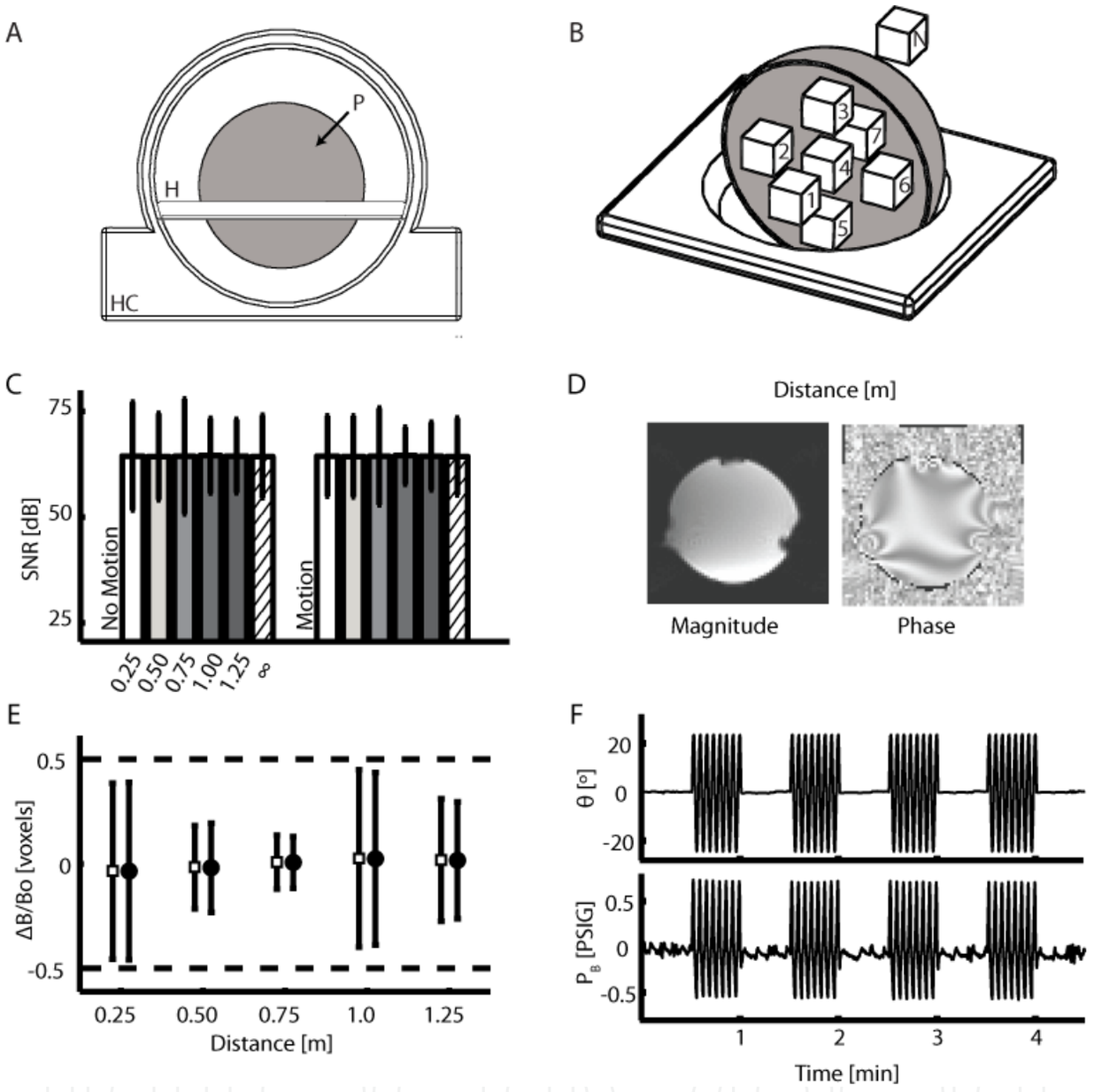

Figure 3. (A) Set-up of the head coil (HC), phantom holder (H), and phantom (P). (B) Holder and phantom cut-away showing details of ROIs used to calculate signal-to-noise ratio (SNR) and field homogeneity. (C) SNR for ROI 3 vs. device operating distance measured from the center of the imaging volume. Error bars represent 95% confidence intervals about the mean SNR at each distance. (D) Sagittal slice of magnitude and phase images of the phantom. Susceptibility artifact in the lower portion of the images was caused by the phantom holder, and was seen in images both with and without the manipulandum in the scanner. (E) Estimate of field homogeneity in ROI 3 from phase data collected in the "No Motion" (open squares) and "Motion" (filled circles) states. We were interested in the distribution of homogeneity values, so error bars in this panel represent ± 2 SD about the mean and thus 95% of the data lie within these bounds. (F) Representative wrist angle and bellows pressure time series collected when the device was 0.50 m from the imaging volume. Angle and pressure measurements are not adversely effected by scanner operation. Figure adapted from Suminski et al., 2007a.

Validation testing used a blocked experimental design (Duration = 270s). During "Motion" states, the computer cycled the device's handle through a sinusoidal trajectory (0.25 cycles per second) whereas the device remained motionless during "No Motion" states (50% duty cycle; period = 60s). Raw, complex k-space data (I and Q channels) were collected to allow analysis of both magnitude and phase MR images. We quantified the effects of simultaneous operation of the robot and scanner during "Motion" and "No Motion" states by imaging the phantom with the robot at 6 distances from the center of the imaging volume (0.25m, 0.50m, 0.75m, 1.0m, and 1.25m) as well as in a control condition with the robot operating in the scanner control room (∞). The phantom was sampled using 7 equal-volume regions of interest (ROI) distributed within its spherical boundary to test whether the robot induced amplitude and phase anisotropies during scanning.

We computed three measures to assess compatibility of the robot and MR scanner; two evaluated MR signal quality during robot operation in the "Motion" and "No Motion" states and the third evaluated the effects of echo planar imaging on measurements of handle position and actuator pressure. First, we calculated the signal to noise ratio (SNR) within each ROI for each robot-distance condition using the magnitude images:

$$SNR_{ROI} = \frac{\mu_{ROI}}{0.665 * \sigma_{noise}} \tag{2}$$

μ_{ROI} is the time series average within a given ROI, and σ_{noise} is an estimate of noise obtained by calculating the standard deviation of the time series in the magnitude images in an identically sized ROI located outside the phantom (Fig. 3B; ROI "N"). The factor 0.665 corrected for changes in the statistical distribution of σ_{noise} caused by calculating the magnitude image from the original complex MR data (Haacke et al., 1999). Values of SNR varied across the seven ROIs but were insensitive to the robot's distance within each ROI (eg. Fig 3C). Three-way ANOVA found main effects of both ROI location ($p < 0.0005$) and robot distance ($p < 0.0005$) but no effect of robot motion state ($p = 0.929$). Comparison of SNR at each of the five distances relative to the control condition (∞) revealed a small but significant 0.64 dB and 0.90 dB *increase* in SNR at 1.0 m and 1.25 m as compared to control ($p < 0.05$), but no change in SNR for the other distances ($p > 0.7$). Thus, we found no systematic degradation of functional MR SNR as a function of robot distance from the imaging volume.

Second, we used the phase images to quantify changes in magnetic field homogeneity induced by robot operation within the scanner suite. We computed the average change in the static magnetic field for each ROI (ΔB_{ROI}):

$$\Delta B_{ROI} = \frac{\phi_{ROI}}{-\gamma T_E} \tag{3}$$

http://dx.doi.org/10.5772/30740

where, ϕ_{ROI} is the average change in each ROI's phase time series with respect to baseline (i.e. ∞), γ is the gyromagnetic ratio, and T_E is the echo time of the EPI sequence (Haacke et al., 1999). We then normalized ΔB_{ROI} to the magnitude of the static magnetic field (B_0 = 3.0T) yielding a unit-less quantity corresponding to the homogeneity of the magnetic field ($\Delta B/B_0$) in parts per million. This normalization process allows comparison of the field homogeneity and the bandwidth/voxel (39Hz or 0.32 ppm) of the EPI sequence. If introduction of the robot into the scanning environment disturbs the field homogeneity by > 0.16 ppm (i.e. ½ voxel), the actual and measured voxel locations would be inconsistent causing inaccuracy in the resultant images. As shown for a representative ROI (Fig. 3B), field inhomogeneity induced by the robot was well below ½ voxel at each distance in the "No Motion" and "Motion" conditions. One-sided t-tests rejected the hypothesis that the field distortion exceeded ½ voxel in either condition ($p < 0.0005$ in each case). Thus, image quality was not compromised by operating the robotic device within the MR scanner.

Finally, we quantified the effects of echo planar imaging on robot operation by calculating SNR for the actuator pressure (SNR_P) and wrist angle (SNR_A) signals while the computer drove the robot's handle through a sinusoidal trajectory:

$$SNR = 20*\log_{10}\left(\frac{RMS_{Signal} - RMS_{Noise}}{RMS_{Noise}}\right) \tag{4}$$

Root mean squared (RMS) values of actuator pressure and joint angle were calculated during "Motion" and "No Motion" states to approximate signal and noise respectively. Neither joint angle nor pressure SNR varied systematically as a function of robot distance from the center of the scanner bore. Individual two-sample t-tests found no difference in SNR_A or SNR_P ($p > 0.705$) when compared to baseline measures obtained when the robot was operated outside the scanning environment (∞).

In conclusion, we have implemented a pneumatically actuated manipulandum that applies controlled joint torques and measures joint angle at the wrist. This device neither degrades fMRI signal quality nor is itself compromised by rapidly switching imaging gradients.

2.3. Comparison of the device with other MR-compatible devices

In the last decade, several robotic devices have been developed for use during MR scanning (see Gassert et al., 2008 for review). The 1 DOF manipulandum we developed compares favorably to other MR-compatible devices used in neuroscience research or rehabilitation applications. For example, the device developed by Hidler et al. (Hidler et al., 2006) only monitors the torque/force generated by a subject whereas our device can simulate dynamic environments by generating controlled torques about the wrist. Other MR-compatible devices can apply dynamic loads using Lorentz coils (Riener et al., 2005), ultrasonic motors (Flueckiger et al., 2005), electrorheological fluids (Khanicheh et al., 2008) or hydrostatic pistons (Gassert et al., 2006). However, in contrast to the device presented by Riener and colleagues, our device does not degrade image quality when operated less than 1m from the scanner's isocenter.

Because the devices presented by Flueckinger (Flueckiger et al., 2005) and Gassert (Gassert et al., 2006) are not backdriveable, they can not simulate realistic dynamic loads during movements requiring rapid changes in direction whereas our device clearly can do so. Recently, Yu, et al. compared 1 DOF MR-compatible devices containing hydraulic and pneumatic actuators (Yu et al., 2008) and concluded that pneumatic actuation was favorable for fast, force controlled applications, whereas hydraulic actuation was best for applications requiring accurate position control (Yu et al., 2008). And while the 2 DOF device presented by Diedrichsen (Diedrichsen et al., 2005) offers the ability to perturb planar reaching movements of the arm, perturbation of proximal limb segments can lead to considerable head motion that must be accounted for during analysis of fMRI data (Diedrichsen and Shadmehr, 2005). In contrast, our current design limits motion to the wrist, which may lead to fewer head motion artifacts in the fMRI dataset.

3. Limb position regulation with proprioceptive feedback

For a first demonstration of the robot's utility, we examined how the brain uses proprioceptive feedback of limb position for the moment-by-moment (i.e. on-line) feedback stabilization of wrist position during a compensatory tracking task. Limb stabilization is important because meaningful interaction with the world frequently requires stabilization of hand-held items (eg. holding a young child's hand) and/or movement of such objects between stabilized positions or "postures" (eg. turning the steering wheel of a car). At any moment, task performance may be compromised due to environmental perturbations (eg. the car hitting a pothole) requiring corrective action to maintain desired performance.

The central nervous system can employ three strategies acting on different timescales to compensate for errors arising during stabilization. First, it may utilize feedback regulation of joint position via segmental (Sinkjaer and Hayashi, 1989) and transcortical ("long loop") reflex pathways (Evarts and Tanji, 1976; Strick, 1978; Evarts and Fromm, 1981) to minimize errors. Alternatively, subjects may increase the impedance of the limb via voluntary co-activation (Milner and Cloutier, 1993) of muscles whose actions oppose one another (i.e. antagonist muscles). Finally, subjects may generate discrete, feedforward, corrective movements when feedback mechanisms and impedance regulation fail to adequately reduce perceived errors (Haaland and Harrington, 1989; Fagg et al., 1998). These strategies are not mutually exclusive, but are complementary in two ways. First, they reduce performance errors over different timescales ranging from the short-latency mechanical responses of antagonist coactivation and reflex action to the reduction of persistent errors by discrete adjustment of behavioral goals. Second, they provide the flexibility in motor output needed to respond to task-dependent tradeoffs between accuracy and muscular effort, thus providing the behavioral basis for optimality in human motor control (Todorov and Jordan, 2002; Scott, 2004). Much is yet unknown about the neuromuscular control of limb position (i.e. posture stabilization), including which aspects of environmental perturbation are compensated on a moment-by-moment basis, and what performance criteria might cause a subject to generate a discrete corrective movement during stabilization.

http://dx.doi.org/10.5772/30740

Ten healthy right-handed volunteers (5 female) participated in two experimental sessions performed on separate days. They performed identical wrist stabilization tasks both days. In one session, subjects stabilized the wrist against robotic perturbation while inside a mock MR scanner. This allowed recording of electromyographic (EMG) data from task-relevant muscles. In the other session, subjects performed the experiment while undergoing FMRI scanning in a 1.5T General Electric Signa scanner equipped with a 3-axis local gradient head coil and an elliptical endcapped quadrature radiofrequency head coil. In both sessions, subjects rested supine in the scanner with their head constrained by foam padding to reduce head motion. With arms at their sides, subjects grasped the robot handle with their right hand. The handle and wrist axes of rotation were aligned and the frame of the device was secured to both the subject's forearm and the inner wall of the scanner bore for support.

3.1. Experimental procedure

Both sessions consisted of a blocked experimental design that alternated between periods of rest and active wrist stabilization. Each stabilization trial was conducted in 5 phases (Fig. 4). During the 30 s prior to stabilization (phase 1), the subject was instructed to relax while the robot held the hand in a comfortable resting posture of 40° flexion (θ_r). 3 s prior to the start of stabilization (phase 2), the robot moved the relaxed hand to the target posture (20° flexion) and held it there until the onset of the stabilization period. The purpose of this phase was to provide a salient haptic cue of the desired wrist angle about which subjects were to stabilize. During the 30 s stabilization period (phase 3), subjects were instructed to hold their wrist steady at the target angle during two experimental conditions in which the device was programmed to apply either a predictable, constant extensor torque about the wrist (*CT*, mean = 1.2 Nm) or unpredictable, pseudo-random extensor torques comprised of band-limited Gaussian "white" noise with a high-frequency cutoff of 1.6 Hz (*RT*; 1.2±1.1 Nm; mean ± SD). At the end of the stabilization period, subjects were instructed to relax while the robot moved the passive hand to its resting position at 40° flexion (phase 4), after which resting EMG continued to be monitored for 3 s (phase 5). Direct view of the wrist was precluded and subjects received no visual feedback of hand motion during stabilization phase 3. Instead, subjects viewed a stationary fixation target that was back-projected onto a screen located at their feet and was visible using prism glasses. The fixation target moved in concert with the hand during passive movement phases 2 and 4 and thus provided an implicit visual representation of the desired wrist angle during stabilization phase 3.

During each 3-minute imaging run, *CT* and *RT* stabilization trials were each presented one time in pseudo-random order, along with 30 s periods of inactivity (rest) preceding and following stabilization. Each subject performed 10 of these runs in each session. Whole-brain images were acquired using a single-shot, blipped gradient-echo echo-planar pulse sequence (19 contiguous sagittal 7-mm slices, TE = 40 ms, TR = 2.5 s, 90° flip angle, FOV = 24 cm, 64x64 matrix, 3.75-mm in-plane resolution). 72 whole-brain images were acquired in each run. BOLD contrast was used to image the hemodynamic related changes in the brain occurring during the two stabilization tasks. Before functional imaging, high-resolution 3D spoiled gradient recalled at steady-state T1-weighted anatomic images were collected for anatomic localization

and co-registration (TE=5 ms, TR=24 ms, 40° flip angle, slice thickness=1.2 mm, FOV=24 cm, 256x192 matrix).

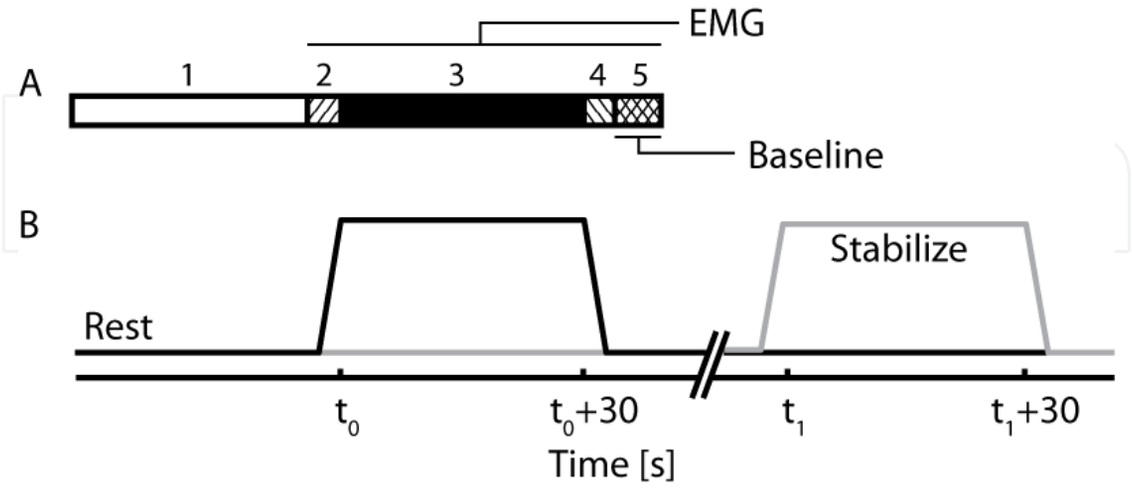

Figure 4. (A) Single stabilization trials were conducted in 5 phases. See text for details. (B) During each imaging run, subjects stabilized their wrist against constant (gray line) or pseudo-random (black line) extensor torque perturbations. Figure adapted from Suminski et al., 2007b.

3.2. Behavioural correlates of stabilization

We found that that wrist torque perturbations elicited changes in wrist angle (θ) and wrist angular velocity ($d\theta/dt$) despite instruction to hold the hand steady. We quantified kinematic performance using the root mean square (RMS) stabilization error. Not unexpectedly, subjects were less able to maintain steady hand posture while perturbed by band-limited pseudo-random torques than by constant torques. Paired t-tests found greater errors in *RT* vs. *CT* trials ($p <= 0.0005$, both sessions). We also observed positional drift over time (a significant slope in the joint angle time series over the final 20 seconds a trial) in 91% of *RT* trials (88 of 96) and 75% of *CT* trials (72 of 95). The absolute magnitude of this drift was 0.155 ± 0.104 °/s and 0.017 ± 0.028 °/s in the *RT* and *CT* cases respectively.

Elevated Coactivity: We quantified coordination between muscles in the arm by estimating the amount of antagonist muscle co-activity at the wrist, elbow and shoulder joints using a coactivity measure also known as 'wasted contraction' (Thoroughman and Shadmehr, 1999) [***C(t)***]. We considered the anterior and postierior deltoid as shoulder antagonists, the biceps and triceps as elbow antagonists, and flexor carpi radialis and extensor carpi radialis as wrist antagonists. ANOVA and post-hoc Dunnet's t-tests found significant elevations in muscle co-activity values (Fig. 5A) during phase 3 ***RT*** stabilization at each joint ($p < 0.0005$) and during phase 3 ***CT*** stabilization at the wrist ($p = 0.03$). No significant EMG activity was observed at any joint during passive movement (phases 2 and 4) when compared to rest.

Feedback Regulation: We evaluated the contributions of reflex-mediated responses to wrist stabilization by analyzing the cross-correlation between wrist angular velocity and measured EMG responses in the ***RT*** condition. For wrist flexor FCR, we consistently observed increased

http://dx.doi.org/10.5772/30740

EMG activity lagging wrist extension by 59.0 ± 44.2 ms (Fig. 5B-d). The timing of this load-dependent activity was within the range of delays expected for transcortical reflex compensation for muscle stretch (Evarts and Vaughn, 1978; Strick, 1978; Matthews, 1981). For wrist extensor ECR, we observed decreased EMG activity lagging wrist extension by 40.3 ± 23.7 ms (Fig. 5B-c). The sign and latency of these EMG changes are consistent with an unloading response mediated by spinal circuits (Sinkjaer et al., 2000). We also observed an increase in ECR activity with lag of 484.8± 118.3 ms (Fig. 5B-e) in 5 out of 10 subjects. This later response is consistent with a strategy of voluntary co-activation about the wrist since no contemporaneous decrease in flexor activity was observed.

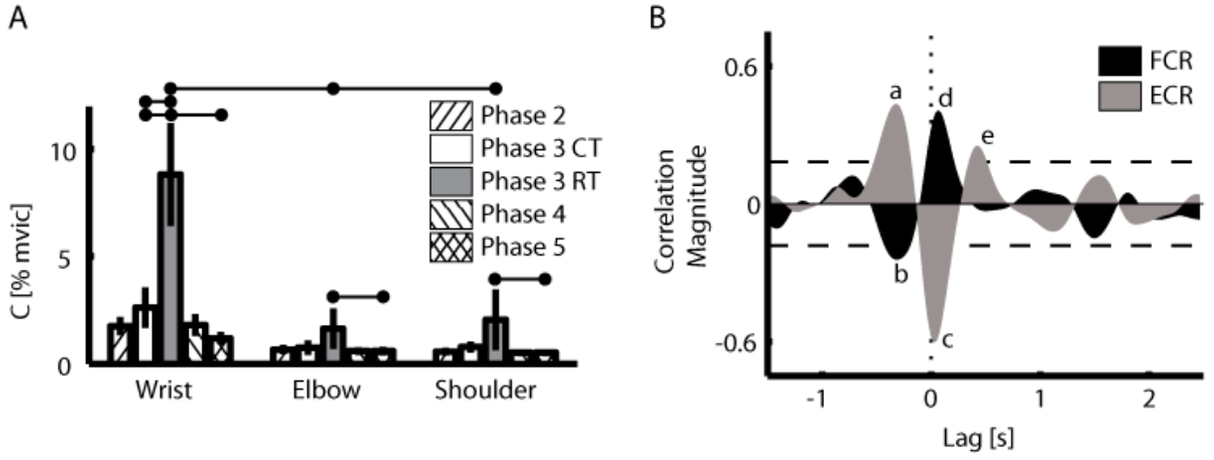

Figure 5. (A) Population average of antagonist muscle coactivity. Horizontal bars indicate significant differences between stabilization conditions ($p < 0.05$). Hatched bars: co-activity during phases 2, 4, and 5. White and gray bars: co-activity during periods of active stabilization against *CT* and *RT* respectively. Error bars indicate ± 2 SEM. (B) Cross-correlation of wrist angular velocity ($d\theta/dt$) and EMG from flexor carpi radialis (*FCR;* black) and extensor carpi radiallis (*ECR*; gray) for a representative subject. Significant correlations were observed with EMG both lagging/leading changes in $d\theta/dt$. Horizontal dashed lines: 95% confidence interval about zero correlation. Figure adapted from Suminski et al., 2007b.

Discrete Corrections: Consistent with expectation, we observed many rapid movements that did not appear to be a direct mechanical consequence of moment-by-moment fluctuations in the robot's commanded wrist torque. To identify the onset of discrete corrective movements, we first computed the average wrist angle trajectory for each subject in each condition. We then removed the trial-averaged trajectory from every individual trial to obtain a 'corrected' wrist angle time series. We considered as discrete corrections only those motions wherein the angular velocity of corrected wrist angle trajectories exceeded 5°/s if they occurred >1 second after the start of stabilization. Discrete corrective movements occurred in 95% of ***RT*** trials (91 of 96) and 19% of ***CT*** trials (18 of 95). The majority of corrective movements were directed appropriately to reduce positioning errors (56.1% and 80% of movements in the ***RT*** and ***CT*** cases, respectively).

In summary, the behavioral and electromyographic data revealed that subjects compensated for environmental perturbations using a combination of three readily identifiable strategies. Subjects modulated limb impedance via co-activation of agonist/antagonist muscle pairs spanning the wrist, elbow and shoulder. Correlation analysis found that subjects also invoke both spinal and supraspinal reflexes to compensate for the perturbations. Finally, subjects generated discrete corrective movements to reduce performance errors that likely accumulated due to the lack of visual feedback during stabilization (cf. Wann and Ibrahim, 1992). We next sought to characterize the neural mechanisms contributing to each of these strategies during experiments conducted within the MR scanner.

3.3. Neural correlates of stabilization

Functional images were generated and analyzed within the Analysis of Functional NeuroImages (AFNI) software package (Cox, 1996). The first three images in each run were discarded to allow for equilibration of the magnetic field. Individual run time series were then concatenated and aligned in three-dimensional space using an interactive, linear, least squares method. Voxel-wise multiple linear regression was used to determine the amount of FMRI signal contrast between the two task conditions (***CT*** and ***RT*** stabilization) and the resting baseline. The resulting functional images for ***RT*** and ***CT*** were interpolated to obtain a volumetric grid having $1mm^3$ voxel volumes, coregistered, and then converted into the Talairach stereotaxic coordinate space (Talairach and Tournoux, 1988). To facilitate group analysis, the Talairached functional images were spatially blurred using a 4-mm Gaussian full-width half-maximum filter to compensate for inter-subject anatomical variability. In all across-subject analyses, a activation volume and thresholding technique was used to correct for multiple comparisons in the group analysis. Appropriate activation volume and individual voxel p-value thresholds ($p=0.005$) were estimated by performing 5000 iterations in a Monte-Carlo simulation using the AlphaSim tool within AFNI (Cox, 1996). The location of activated regions in group statistical parametric maps was obtained using the Talairach atlas (Talairach and Tournoux, 1988) for cerebral activations and the Schmahmann atlas (Schmahmann, 2000) for activations in the cerebellum and its nuclei. Cortical activations were visualized using CARET (Van Essen et al., 2001); http://brainmap.wustl.edu/caret).

Changes in BOLD signal intensity (relative to rest) correlated with periods of ***CT*** or ***RT*** stabilization in many brain regions that contribute to control of the upper extremity (Table 1; Fig. 6A). We visualized the time series of BOLD activations for each ROI during stabilization against each load type for each subject. Two patterns of activation became evident. The first, an example of which is shown for an ROI spanning left primary motor and somatosensory cortices (Fig. 6B; M1/S1), was characterized by increases in percentage BOLD signal intensity change (PSC) throughout the ***RT*** stabilization periods and during the passive hand movements preceding and following ***CT*** stabilization. Motion sensitivity during active stabilization and passive movement might be expected from brain regions concerned with the estimation of - and on-line feedback correction for - performance errors (Marsden et al., 1972; Lee and Tatton, 1975; Evarts and Vaughn, 1978; Marsden et al., 1978; Strick, 1978; Horne and Butler, 1995; Scott, 2004). This idea is based on the assumption that passive movement of the wrist induces a

http://dx.doi.org/10.5772/30740

discrepancy (error) between actual limb position and that expected given the recent history of motor output. The second pattern, an example is shown for the right middle frontal gyrus (Fig. 6B; BA 46), was characterized by a parallel increase in PSC during both stabilization conditions with no sensitivity to passive movement. This pattern might be expected from regions (i.e. prefrontal cortex, anterior cingulate cortex, rostral aspects of dorsal premotor and SMA cortices, and inferior aspects of posterior parietal cortex) involved in supervisory aspects of control such as evaluating the success of an ongoing task (Carter et al., 1998) as well as the resetting of behavioral goals when ongoing performance is deficient (Jahanshahi et al., 1995; Winstein et al., 1997; Jueptner and Weiller, 1998; Sakai et al., 1999). As shown for an ROI in the cerebellum (Fig 6B, CBLM), some regions exhibited an intermediate pattern (i.e. some sensitivity to stabilization type but little sensitivity to passive movement). To quantify these observations, we defined a 2-element feature vector $\Psi = \{\bar{S}, \Delta_M\}$ summarizing the average increase in PSC induced by passive movement in phase 2 ($\bar{S}$) and the difference in PSC between ***RT*** and ***CT*** trials during stabilization (Δ_M). The $\bar{S}$ feature was the average of 4 consecutive TR samples from each of the ***RT*** and ***CT*** trials, beginning 5 seconds (i.e. 2 TR) prior to the start of the stabilization period. The Δ_M feature was computed as the difference between the average ***RT*** and ***CT*** PSC time series during the middle 20 seconds (8 TR) of stabilization.

Using these features, we performed a k-means cluster analysis to identify ROIs demonstrating common patterns of sensitivity to trial type and/or passive movement. Two distinct groups were identified: ROIs that were sensitive to both trial type and passive movement (Cluster I; red regions in Fig. 6A), and those demonstrating increased BOLD activation over the duration of the trial with little sensitivity to passive movement (Cluster II; blue regions in Fig. 6A). Group separation and membership was visualized by plotting the coordinates of each ROI on the axes defined by the features of Ψ (Fig. 6C; Cluster I = red circles; Cluster II = blue squares). Regions showing significant sensitivity to passive movement ($\bar{S} \neq 0$; $p < 0.05$) are indicated by filled symbols. These include left M1/S1, SPL/IPL (BA 5 and 7), and SMA/CCZ. The left M1/S1, SPL/IPL (BA 5 and 7), and right STG (BA 39) were also significantly modulated by task type ($\Delta_M > 0$; $p < 0.05$). ROIs with membership in Cluster I were characterized by both a high sensitivity to trial type (being more active during RT trials) and a robust response to passive movement of the wrist. Such sensitivity to positioning errors is necessary for regions directly involved in the feedback control of movement kinematics (i.e. limb position, velocity and acceleration). Indeed, responsivity to passive movement has been considered a hallmark of brain regions participating in the optimal feedback control of movement (Scott, 2004). In contrast, Cluster II ROIs exhibited generally elevated BOLD activation during stabilization with little sensitivity to trial type or passive movement. This pattern of activity is expected from regions involved in supervisory aspects of control rather than in the moment-by-moment cancellation of position errors.

We performed a second BOLD regression analysis to identify brain regions involved in generating the discrete corrective movements observed behaviorally. We limited our investigation to the ***CT*** stabilization blocks because corrections were unambiguous and most often directed to decrease kinematic error. In particular, we wished to know whether the regions generating corrective movements might be a subset of the networks previously described or

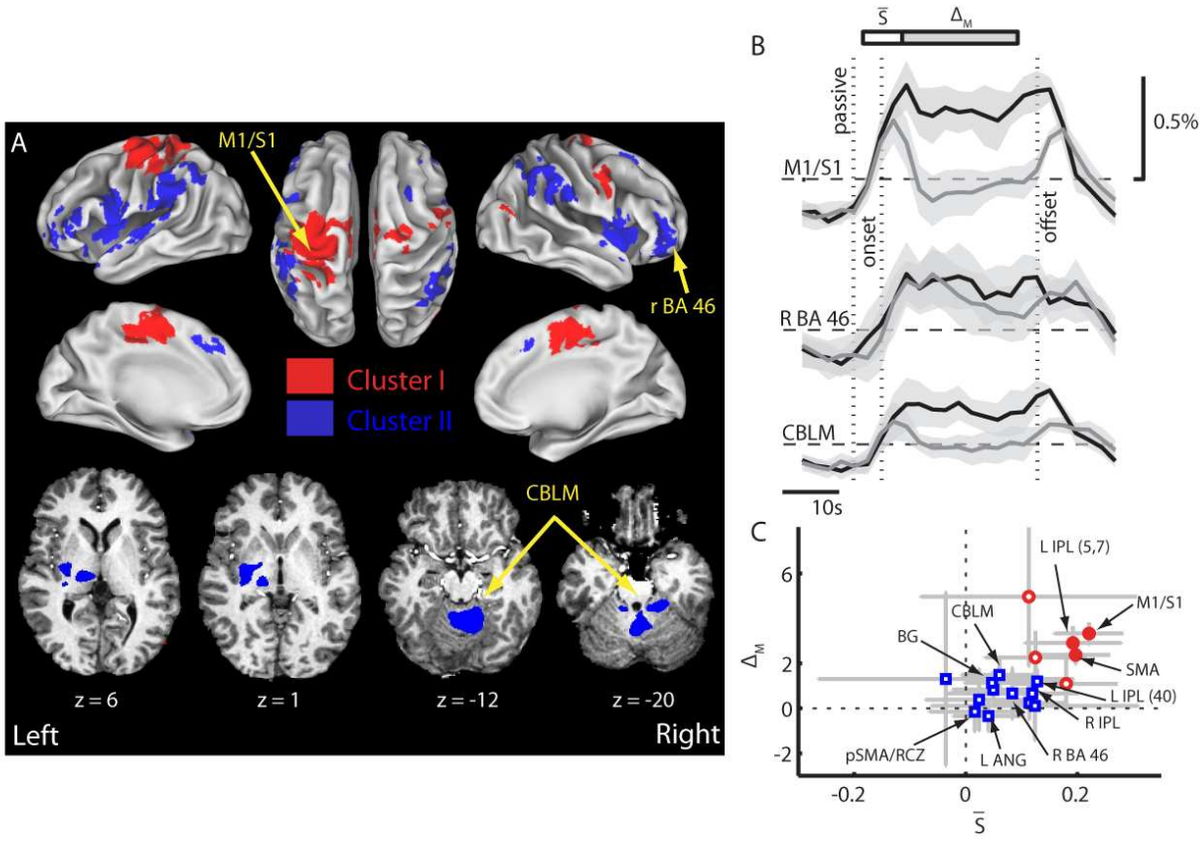

Figure 6. (A) Population maps showing significantly activated ROIs during periods of random ***RT*** or constant ***CT*** stabilization ($p < 0.05$; corrected for multiple comparisons). Cluster I ROIs are shown in red while Cluster II ROIs are shown in blue. Upper panels: activations mapped onto inflated representations of the cerebral hemispheres. Lower panels: activations in the basal ganglia, thalamus, cerebellar cortex (lobule IV-VI), and right dentate nucleus. (B) Percent signal change (PSC) of BOLD time series from ***RT*** (black) and ***CT*** (gray) stabilization periods. Shaded regions: ±2 SEM. Scale bars above the PSC plots indicate the time intervals used to calculate the components of $\Psi = \{\bar{S}, \Delta_M\}$. (C) Group membership for 18 ROIs was visualized by plotting the coordinates of each ROI within the plane defined by the features of Ψ (red: Cluster I; blue: Cluster II). Filled symbols: region where PSC differs significantly from resting baseline. Figure reproduced with permission from Suminski et al., 2007b.

different networks. For this event-related analysis, we created input reference functions for each subject indicating the onset times of discrete corrective movements during ***CT*** stabilization. These time series had a value of 1 during each sampling instant (TR) wherein a discrete corrective movement occurred and 0 otherwise. Additional reference time series were included to mitigate effects of head motion and to model the average activity used to maintain limb position during CT stabilization. Regressors were convolved with a γ-variate function and the resulting functional images were pre-processed as described above. Voxel-wise, one-sided t-tests found specific regions in Cluster I and Cluster II to be modulated discrete movement corrections. Interestingly, BOLD signal intensity *increased* with respect to baseline in a subset of regions in Cluster II, while a subset of regions in Cluster I exhibited BOLD signal *decreases* (Fig. 7; red and blue areas, respectively). These results highlight the manner in which Cluster I and II regions work together to maintain the position of the limb during stabilization against a deterministic perturbation: During CT trials, discrete corrective movements induce a

http://dx.doi.org/10.5772/30740

		Tailarach Coordinates				
	Hem	**X**	**Y**	**Z**	**Vol**	**Mean T**
Cluster I						
Precentral Gyrus (BA 4,6)	L	-30.1	-19.4	51.3	14166	5.884
Medial Frontal Gyrus (BA 6)	B	-0.5	-11.6	48	7856	5.0334
Cingulate Gyrus (BA 24,31)						
Inferior/Superior Parietal Lobule (BA 5,7,40)	L	-30.3	-38.3	56.6	2630	4.7958
Precentral Gyrus (BA 6)	R	49.6	-2.4	39	957	4.5288
Precentral Gyrus (BA 6)	R	22.3	-15.4	61.2	866	4.2839
Middle Temporal Gyrus (BA 39)	R	52.6	-68.9	15.9	596	4.3556
Cluster II						
Cortical						
Insula (BA 13)	L	-47.5	0.2	8.3	8102	4.8657
Superior Temporal Gyrus (BA 22,41)						
Inferior Parietal Lobule (BA 40)	L	-50.9	-31.5	24.9	7477	4.9995
Insula (BA 13)	R	42.7	5.6	4.8	5633	5.0229
Superior Temporal Gyrus (BA 22)						
Inferior Parietal Lobule (BA 40)	R	53.4	-40.6	36.4	5125	4.3849
Supramarginal Gyrus						
Middle/Inferior Frontal Gyrus (BA 10,46)	R	39.2	38.5	3.5	2668	4.5259
Middle/Inferior Frontal Gyrus (BA 10,45,46)	L	-42	29.8	12.5	1334	4.3385
Inferior Parietal Lobule (BA 40)	L	-49.1	-53.3	39.9	1079	4.1923
Angular Gyrus						
Medial Frontal Gyrus (BA 6,8)	B	-3	25.4	41.5	1033	4.156
Cingulate Gyrus (BA 32)						
Superior Frontal Gyrus (BA 8)						
Superior Frontal Gyrus (BA 6)	R	22.1	13.3	51.6	687	4.5912
Middle Frontal Gyrus (BA 10)	L	-38.2	49.2	3.4	582	4.2741
Subcortical and Cerebellum						
Cerebellar Cortex Lobule IV, V, VI	B	5.9	-49.4	-14	9571	5.2885
Dentate	R					
Basal Ganglia and Thalamus	L	-19.7	-17	10.1	6684	5.025
L = Left; R = Right; B = Bilateral; BA = Broadman's Area						

Table 1. Brain regions exhibiting significant task-related activation during ***RT*** or ***CT*** trials.

persistent decrease in the magnitude of kinematic errors, thus reducing the need for feedback regulation of position and likely contributing to the inhibition of Cluster I ROIs. Conversely, we found the BOLD activity increased in a subset of Cluster II ROIs at the specific times when discrete movements were performed. Such behavior would be expected from brain regions involved in the resetting of behavioral goals (reference wrist angle) when performance is deficient.

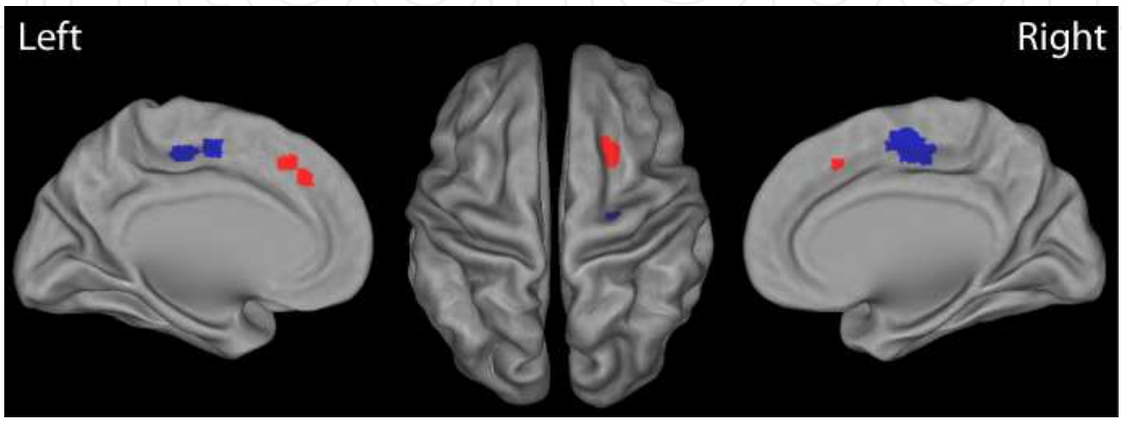

Figure 7. Activation maps showing regions where BOLD signal correlated with the generation of discrete corrective movements ($p < 0.05$, corrected for multiple comparisons). Increased BOLD activiy was observed in a subset of Cluster II regions [red: right pre-PMd, left medial frontal gyrus (BA 8) and rostral cingulate]. BOLD activaions decreased relative to resting state activity in Cluster I regions (blue: bilateral SMA and right PMd).

We performed a final set of multiple linear regression analyses to identify brain regions explicitly involved in the moment-by-moment and long-term evaluation and correction for kinematic and/or kinetic performance errors. We wished to know whether the activations identified in the preceding analyses were related to compensation for kinematic errors, generation of wrist torques, or both. Here, we performed four separate regressions using input reference functions corresponding to the magnitude of RMS wrist angle errors and RMS torque both on a trial-by-trial and TR-by-TR basis ($\boldsymbol{Error}_{Trial}$, $\boldsymbol{Error}_{TR}$, $\boldsymbol{Torque}_{Trial}$, and $\boldsymbol{Torque}_{TR}$). Each function was created from error or pressure data measured during the corresponding stabilization run within the MR-scanner. The value at each (TR) sampling instant for $\boldsymbol{Error}_{Trial}$ and $\boldsymbol{Torque}_{Trial}$ was set equal to the RMS error (or torque) value computed throughout the corresponding stabilization period (30 s integration window). The value at each (TR) sampling instant for $\boldsymbol{Error}_{TR}$ and $\boldsymbol{Torque}_{TR}$ (reference functions that varied on a moment-by-moment basis) was set equal to the RMS error (torque) value computed during that TR sampling period (2.5 s integration window). In all cases, the reference time series were convolved with a γ-variate function to model the temporal filtering properties of the hemodynamic response. Additional reference time series included head motion parameters and functions representing periods of ***RT*** and ***CT*** stabilization. The resulting functional images were processed as described above.

http://dx.doi.org/10.5772/30740

Voxel-wise, one-sided t-tests were used to identify regions where BOLD signal covaried with $Error_{Trial}$, $Error_{TR}$, $Torque_{Trial}$, or $Torque_{TR}$.

Regions demonstrating increased sensitivity to errors that change on a moment-by-moment timescale ($Error_{TR}$; Fig. 8 red) were predominantly members of Cluster I, while regions sensitive to kinematic errors on a much longer timescale ($Error_{Trial}$; Fig. 8 blue) were more likely to be members of Cluster II (see also Table 2). Activation of the left IPL in the $Error_{Trial}$ contrast was located more posterior to those activated regions of IPL in the $Error_{TR}$ contrast. There were no overlapping activations in the $Error_{Trial}$ and $Error_{TR}$ contrasts. Importantly, no regions were found to be active in contrasts examining differences between either $Torque_{Trial}$ or $Torque_{TR}$ and resting baseline.

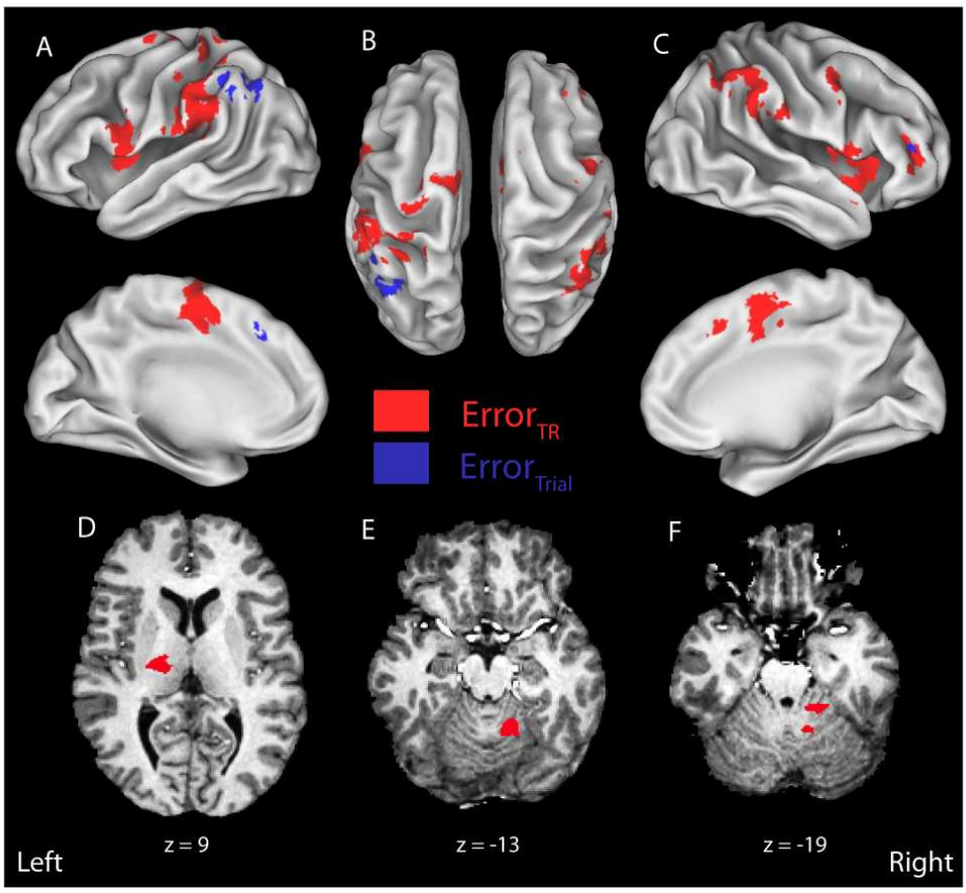

Figure 8. Activation maps showing regions wherein the BOLD response correlated with kinematic performance errors (i.e. state estimation errors) on both a moment-by-moment ($Error_{TR}$, red regions) and a trial-by-trial basis ($Error_{Trial}$, blue regions) ($p < 0.05$, corrected for multiple comparisons). Figure reproduced with permission from Suminski et al., 2007b.

		Tailarach Coordinates				
	Hem	**X**	**Y**	**Z**	**Vol**	**Mean T**
ErrorTR						
Cortical						
Inferior Parietal Lobule (BA 40)	L	51.3	29.9	28.4	3599	4.7941
Supramarginal Gyrus						
Postcentral Gyrus (BA 2)						
Insula (BA 13)						
Medial Frontal Gyrus (BA 6)	B	1.5	4.9	50	3056	4.7047
Superior Frontal Gyurs (BA 6)	L					
Cingulate Gyrus (BA 24)	R					
Insula (BA 13)	R	-41	-8.3	2.9	2245	4.7498
Superior Temporal Gyrus (BA 22)						
Insula (BA 13)	L	47	-0.5	11.8	1986	4.9146
Superior Temporal Gyrus (BA 22)						
Inferior Parietal Lobule (BA 40)	R	-50.4	42	38.7	1706	4.2648
Supramarginal Gyrus						
Inferior Parietal Lobule (BA 5,40)	L	35.6	38.4	53.3	761	4.2931
Inferior Frontal Gyrus (BA 46)	R	-35.7	-34.5	14.9	756	5.0422
Middle Frontal Gyurs (BA 10)						
Precentral Gyrus (BA 6)	R	-46.3	2.3	43	247	4.7634
Precentral Gyrus (BA 44)	R	-53.7	-5.6	9.8	180	4.0774
Cingulate Gyrus (BA 32)	R	-8.6	-17.8	43.7	152	5.0572
Precentral Gyrus (BA 4)	L	28.5	21.6	63.2	115	3.9996
Subcortical and Cerebellum						
Basal Ganglia and Thalamus	L	18.8	14.4	7.1	1036	4.4593
Putamen						
Globus Pallidus (Medial/Lateral)						
Ventral Posterior Lateral						
Ventral Lateral						
Cerebellar Cortex Lobule IV, V, VI	R	-15.4	48.5	-16.1	871	4.2192
Dentate						
ErrorTrial						
Inferior Parietal Lobule (BA 40)	L	41.5	54.3	36.6	556	4.302
Supramarginal Gyrus						
Medial Frontal Gyrus (BA 8)	L	6.9	-20.3	43.6	45	3.9183
L = Left; R = Right; B = Bilateral; BA = Broadman's Area						

Table 2. Brain regions activated in the $Error_{TR}$ and $Error_{Trial}$ contrasts.

http://dx.doi.org/10.5772/30740

4. Summary and future directions

This chapter has described the development and validation of a novel, 1 DOF pneumatically actuated manipulandum. We demonstrated that the device was: 1) capable of generating computer controlled perturbations of movement and 2) compatible with the MR scanner such that performance of neither the device nor image quality was affected by robot operation. We then demonstrated device utility in a study of wrist posture stabilization against environmental perturbation. We provided behavioral evidence that subjects invoke three complementary compensatory responses when stabilizing the wrist in the absence of ongoing visual feedback of task performance. These compensatory responses include feedback regulation via spinal and long-loop reflexes, impedance modulation via antagonist muscle co-activation and feedforward, discrete corrective movements. Analysis of functional neuroimages obtained from the same subjects performing the same tasks revealed two distinct networks that were differentially excited by the task. The first (Cluster I) included a cerebello-thalamo-cortical network previously implicated in the online computation and feedback correction of errors (Marsden et al., 1972; Lee and Tatton, 1975; Evarts and Vaughn, 1978; Marsden et al., 1978; Strick, 1978; Horne and Butler, 1995). BOLD signal changes within these regions were correlated with moment-by-moment fluctuations in state estimation errors (Fig. 7, red regions; $\boldsymbol{Error}_{TR}$, 2.5 s integration period). That is, BOLD activity in these regions was elevated mainly during random torque perturbations and during passive movement of the hand, despite the absence of significant muscle activation during passive manipulation in the behavioral experiments and the production of the same average wrist torques in both tasks. A second network (Cluster II) exhibited similarly elevated BOLD activity during performance of both stabilization tasks. Brain regions demonstrating this pattern include the prefrontal cortex, rostral aspects of dorsal premotor and SMA cortices, and inferior aspects of posterior parietal cortex. These brain regions have previously been reported to contribute to the planning and execution of internally-generated, discrete motor actions (Jahanshahi et al., 1995; Winstein et al., 1997; Jueptner and Weiller, 1998; Sakai et al., 1999). Consistent with those reports, we found that BOLD activity increased within rostral PMd, SMA and cingulate cortex during time periods wherein subjects generated discrete corrective movements. Although discrete corrections were transient events, they gave rise to long-lasting performance improvements in most cases and so, they likely represent a resetting of the reference wrist angle when online (moment-by-moment) feedback control failed to satisfy subjective performance constraints. To do so, however, subjects first needed to determine when error had grown sufficiently large to warrant correction and then plan the direction and magnitude of corrective action. This type of supervisory role likely was supported by Cluster II ROIs demonstrating high sensitivity to state estimation errors over a longer, 30 s timeframe (Fig. 7, blue regions).

These results highlight the importance of both postural and movement trajectory control mechanisms in peripheral limb stabilization and suggest a possible neural basis for the distinct postural and trajectory (movement) control mechanisms recently isolated during point-to-point arm movements and movement sequences (Ghez et al., 2007; Scheidt and Ghez, 2007). Additional studies are needed to better understand how the brain combines the different control processes to minimize performance errors and how the brain uses information from

multiple sensory feedback modalities to optimize limb stabilization and movement control. Such work will be greatly facilitated by the use of mechanically-active tools that apply physical perturbations to the limb while subjects undergo concurrent functional MR imaging.

Acknowledgements

This work was supported by NSF BES0238442, NIH NCRR M01-RR00058, 2 P01 MH51358, R01 HD053727 and by the Alvin W. and Marion Birnschein Foundation. We thank Kristine Mosier and Steve Rao for constructive feedback on an earlier version of this manuscript, Jeff Goldstein for crafting the manipulandum, Dr. N. Bansal for helpful suggestions regarding the statistical handling of the data, as well as Vanai Roopchansingh, Sally Durgerian, Matthew Verber and the MCW MRI technicians for assistance during FMRI data collection and analysis.

Author details

Aaron J. Suminski[1,2] and Robert A. Scheidt[1,3,4]

1 Biomedical Engineering, Marquette University, Milwaukee, WI, USA

2 Organismal Biology and Anatomy, University of Chicago, Chicago, IL, USA

3 Neurology, Medical College of Wisconsin, Milwaukee, WI, USA

4 Physical Medicine and Rehabilitation, Feinberg School of Medicine, Northwestern University, Chicago, IL, USA

References

[1] Carter CS, Braver TS, Barch DM, Botvinick MM, Noll D, Cohen JD (1998) Anterior cingulate cortex, error detection, and the online monitoring of performance. Science 280:747-749.

[2] Chinzei K, Kikinis R, Jolesz FA (1999) MR compatibility of mechatronic devices: design criteria. In: Medical Image Computing and Computer-Assisted Intervention Meeting - MICCAI'99., pp 1020-1030. Cambridge, UK.

[3] Cox RW (1996) AFNI: software for analysis and visualization of functional magnetic resonance neuroimages. Comput Biomed Res 29:162-173.

[4] Diedrichsen J, Shadmehr R (2005) Detecting and adjusting for artifacts in fMRI time series data. Neuroimage 27:624-634.

[5] Diedrichsen J, Hashambhoy Y, Rane T, Shadmehr R (2005) Neural correlates of reach errors. J Neurosci 25:9919-9931.

[6] Evarts EV, Tanji J (1976) Reflex and intended responses in motor cortex pyramidal tract neurons of monkey. J Neurophysiol 39:1069-1080.

[7] Evarts EV, Vaughn WJ (1978) Intended Arm Movements in Response to Externally Produced Arm Displacements in Man. In: Cerebral Motor Control in Man: Long Loop Mechanisms (Desmedt JE, ed), pp 178-192. Basel ; New York: Karger.

[8] Evarts EV, Fromm C (1981) Transcortical reflexes and servo control of movement. Can J Physiol Pharmacol 59:757-775.

[9] Fagg AH, Barto AG, Houk JC (1998) Learning to reach via corrective movements. In: Tenth Yale Workshop on Adaptive and Learning Systems, pp pp. 179-185. New Haven, CT.

[10] Flueckiger M, Bullo M, Chapuis D, Gassert R, Perriard Y (2005) fMRI compatible haptic interface actuated with traveling wave ultrasonic motor. In: IEEE Industry Applications Society Fortieth Annual Meeting pp 2075-2082 2073. Kowloon, Hong Kong.

[11] Ganesh G, Gassert R, Burdet E, Bleuler H (2004) Dynamics and control of an MRI compatible master-slave system with hydrostatic transmission. In: IEEE International Conference on Robotics and Automation, pp 1288-1294. New Orleans, LA.

[12] Gassert R, Burdet E, Chinzei K (2008) Opportunities and challenges in MR-compatible robotics: reviewing the history, mechatronic components, and future directions of this technology. IEEE Eng Med Biol Mag 27:15-22.

[13] Gassert R, Moser R, Burdet E, Bleuler H (2006) MRI/fMRI-compatible robotic system with force feedback for interaction with human motion. IEEE/ASME Transactions on Mechatronics 11:216-224.

[14] Ghez C, Scheidt R, Heijink H (2007) Different learned coordinate frames for planning trajectories and final positions in reaching. J Neurophysiol 98:3614-3626.

[15] Haacke EM, Brown RW, Thompson MR, Venkatesan R (1999) Magnetic resonance imaging : physical principles and sequence design. New York: Wiley.

[16] Haaland KY, Harrington DL (1989) Hemispheric control of the initial and corrective components of aiming movements. Neuropsychologia 27:961-969.

[17] Hidler J, Hodics T, Xu B, Dobkin B, Cohen LG (2006) MR compatible force sensing system for real-time monitoring of wrist moments during fMRI testing. J Neurosci Methods 155:300-307.

[18] Horne MK, Butler EG (1995) The role of the cerebello-thalamo-cortical pathway in skilled movement. Prog Neurobiol 46:199-213.

[19] Imamizu H, Miyauchi S, Tamada T, Sasaki Y, Takino R, Putz B, Yoshioka T, Kawato M (2000) Human cerebellar activity reflecting an acquired internal model of a new tool.[comment]. Nature 403:192-195.

[20] Jahanshahi M, Jenkins IH, Brown RG, Marsden CD, Passingham RE, Brooks DJ (1995) Self-initiated versus externally triggered movements. I. An investigation using measurement of regional cerebral blood flow with PET and movement-related potentials in normal and Parkinson's disease subjects. Brain 118 (Pt 4):913-933.

[21] Jueptner M, Weiller C (1998) A review of differences between basal ganglia and cerebellar control of movements as revealed by functional imaging studies. Brain 121 (Pt 8):1437-1449.

[22] Kawato M, Kuroda T, Imamizu H, Nakano E, Miyauchi S, Yoshioka T (2003) Internal forward models in the cerebellum: fMRI study on grip force and load force coupling. Progress in Brain Research 142:171-188.

[23] Khanicheh A, Mintzopoulos D, Weinberg B, Tzika AA, Mavroidis C (2008) MR_CHIROD v.2: magnetic resonance compatible smart hand rehabilitation device for brain imaging. IEEE Trans Neural Syst Rehabil Eng 16:91-98.

[24] Khanicheh A, Muto A, Triantafyllou C, Weinberg B, Astrakas L, Tzika A, Mavroidis C (2005) MR compatible ERF driven hand rehabilitation device. In: IEEE 9th International Conference on Rehabilitation Robotics, pp 7-12. Chicago, IL.

[25] Lee RG, Tatton WG (1975) Motor responses to sudden limb displacements in primates with specific CNS lesions and in human patients with motor system disorders. Can J Neurol Sci 2:285-293.

[26] Marsden CD, Merton PA, Morton HB (1972) Servo action in human voluntary movement. Nature 238:140-143.

[27] Marsden CD, Merton PA, Morton HB, Adam JER, Hallett M (1978) Automatic and Voluntary Responses to Muscle Stretch in Man. In: Cerebral Motor Control in Man: Long Loop Mechanisms (Desmedt JE, ed), pp 167-177. Basel ; New York: Karger.

[28] Matthews PBC (1981) Muscle spindles their messages and their fusimotor supply. In: Sect, 1: The Nervous System (Brookhart JM, Mountcastle VB, Brooks VB, eds), pp 189-228. Bethesda: Am. Phisiol. Soc.

[29] Milner TE, Cloutier C (1993) Compensation for mechanically unstable loading in voluntary wrist movement. Experimental Brain Research 94:522-532.

[30] Peck KK, Sunderland A, Peters AM, Butterworth S, Clark P, Gowland PA (2001) Cerebral activation during a simple force production task: changes in the time course of the haemodynamic response. Neuroreport 12:2813-2816.

[31] Rao SM, Bandettini PA, Binder JR, Bobholz JA, Hammeke TA, Stein EA, Hyde JS (1996) Relationship between finger movement rate and functional magnetic reso-

nance signal change in human primary motor cortex. J Cereb Blood Flow Metab 16:1250-1254.

[32] Riener R, Villgrattner T, Kleiser R, Nef T, Kollias S (2005) fMRI-Compatible Electromagnetic Haptic Interface. In: 27th Annual International Conference of the IEEE-EMBS, pp 7024-7027. Shanghi, China.

[33] Sakai K, Hikosaka O, Miyauchi S, Sasaki Y, Fujimaki N, Putz B (1999) Presupplementary motor area activation during sequence learning reflects visuo-motor association. J Neurosci 19:RC1.

[34] Scheidt RA, Ghez C (2007) Separate adaptive mechanisms for controlling trajectory and final position in reaching. J Neurophysiol 98:3600-3613.

[35] Schenck JF (1996) The role of magnetic susceptibility in magnetic resonance imaging: MRI magnetic compatibility of the first and second kinds. Medical Physics 23:815-850.

[36] Schmahmann JD (2000) MRI atlas of the human cerebellum. In. San Diego: Academic Press.

[37] Scott SH (2004) Optimal feedback control and the neural basis of volitional motor control. Nat Rev Neurosci 5:532-546.

[38] Sinkjaer T, Hayashi R (1989) Regulation of wrist stiffness by the stretch reflex. J Biomech 22:1133-1140.

[39] Sinkjaer T, Andersen JB, Ladouceur M, Christensen LO, Nielsen JB (2000) Major role for sensory feedback in soleus EMG activity in the stance phase of walking in man. J Physiol 523 Pt 3:817-827.

[40] Strick PL (1978) Cerebellar Involvement in 'Volitional' Muscle Responses to Load Changes. In: Cerebral Motor Control in Man: Long Loop Mechanisms (Desmedt JE, ed), pp 85-93. Basel ; New York: Karger.

[41] Suminski AJ, Ropella KM, Scheidt RA (2002) A pneumatically actuated manipulandum for neuromotor control research. In: IEEE EMBS Society Meeting, pp 2347-2348 vol.2343. Houston, TX.

[42] Suminski AJ, Zimbelman JL, Scheidt RA (2007a) Design and validation of a MR-compatible pneumatic manipulandum. J Neurosci Methods 163:255-266.

[43] Suminski AJ, Rao SM, Mosier KM, Scheidt RA (2007b) Neural and electromyographic correlates of wrist posture control. J Neurophysiol 97:1527-1545.

[44] Talairach J, Tournoux P (1988) Co-planar stereotaxic atlas of the human brain. Stuttgart/New York: Thieme.

[45] Thoroughman KA, Shadmehr R (1999) Electromyographic correlates of learning an internal model of reaching movements. J Neurosci 19:8573-8588.

[46] Todorov E, Jordan MI (2002) Optimal feedback control as a theory of motor coordination. Nat Neurosci 5:1226-1235.

[47] Vaillancourt DE, Thulborn KR, Corcos DM (2003) Neural basis for the processes that underlie visually guided and internally guided force control in humans. J Neurophysiol 90:3330-3340.

[48] Van Essen DC, Drury HA, Dickson J, Harwell J, Hanlon D, Anderson CH (2001) An integrated software suite for surface-based analyses of cerebral cortex. J Am Med Inform Assoc 8:443-459.

[49] Wann JP, Ibrahim SF (1992) Does limb proprioception drift? Exp Brain Res 91:162-166.

[50] Winstein CJ, Grafton ST, Pohl PS (1997) Motor task difficulty and brain activity: investigation of goal-directed reciprocal aiming using positron emission tomography. J Neurophysiol 77:1581-1594.

[51] Yu N, Hollnagel C, Blickenstorfer A, Kollias SS, Riener R (2008) Comparison of MRI-Compatible Mechatronic Systems With Hydrodynamic and Pneumatic Actuation. Mechatronics, IEEE/ASME Transactions on 13:268-277.

[52] Ziegler JG, Nichols NB (1942) Optimum settings for automatic controllers. ASME Trans 64:759-768.